

Contents lists available at ScienceDirect

Petroleum Science

journal homepage: www.keaipublishing.com/en/journals/petroleum-science



Original Paper

Experimental investigation on cross-layer propagation of hydraulic fractures in shale-sandstone interbedded reservoirs



Chao Liu ^{a, b}, Hai-Yan Zhu ^{a, b, *}, Kai Tang ^c, Peng Zhao ^{a, b}, Xuan-He Tang ^{a, b}, Lei Tao ^{a, b}, Zhao-Peng Zhang ^{a, b}, Guo-Hui Ren ^c

- ^a College of Energy, Chengdu University of Technology, Chengdu, 610059, Sichuan, China
- b State Key Laboratory of Oil and Gas Reservoir Geology and Exploitation, Chengdu University of Technology, Chengdu, 610059, Sichuan, China
- ^c Southwest Branch, CNPC China Petroleum Logging Company Limited, Chongqing, 401120, China

ARTICLE INFO

Article history: Received 29 October 2024 Received in revised form 17 April 2025 Accepted 17 April 2025 Available online 17 April 2025

Edited by Yan-Hua Sun

Keywords: Interbedded reservoir Shale oil and gas Hydraulic fracturing Fracture propagation Acoustic emission

ABSTRACT

China's shale oil and gas resources are widely distributed in shale-sandstone interbedded reservoirs. whose complex lithology and strong heterogeneity pose significant challenges to hydraulic fracturing design. To address issues such as the difficulty in controlling fracture height and the challenge of forming an effective fracture network, this study utilizes synthetic rock samples that can represent the characteristics of interbedded reservoirs and investigates the initiation and propagation of hydraulic fractures under different viscosity, injection rate, and construction scheme. By combining real-time monitoring of injection pressure with acoustic emission, the temporal and spatial evolution characteristics of hydraulic fractures as well as the mechanisms of their vertical and horizontal extension are revealed. The results indicate that a higher fracturing fluid viscosity is essential for ensuring the vertical cross-layer propagation of hydraulic fractures, while a lower fluid viscosity facilitates the activation of weak interlayer surfaces, promoting sufficient horizontal propagation along these planes and forming branched fractures. Although a higher injection rate enhances the vertical cross-layer propagation of hydraulic fractures, it also causes greater diversion of the main fracture plane, resulting in simpler fracture morphology and limiting the stimulation effect. Additionally, an alternating injection of high and low viscosity fracturing fluids allows hydraulic fractures to both break through weak interlayer surfaces and achieve uniform horizontal propagation, resulting in a more complex fracture morphology. The findings are expected to provide a scientific basis and practical guidance for optimizing hydraulic fracturing designs in interbedded reservoir conditions.

© 2025 The Authors. Publishing services by Elsevier B.V. on behalf of KeAi Communications Co. Ltd. This is an open access article under the CC BY license (http://creativecommons.org/licenses/by/4.0/).

1. Introduction

Shale oil and gas, as an important supplement to conventional oil and gas resources, play an increasingly significant role in the energy structure (Muther et al., 2022; Dong et al., 2025). Shale oil and gas are typically found in interbedded reservoirs, which require production enhancement techniques such as hydraulic fracturing for extraction and utilization (Yu et al., 2024). Due to the strong heterogeneity and complex lithology of interbedded reservoirs, hydraulic fracturing faces significant challenges (Li et al., 2015; Zhu et al., 2023; Zhou et al., 2024). For instance, excessive vertical propagation of hydraulic fracture (HF) can breach caprocks or

barriers, causing treatment pressure to diffuse into adjacent layers, and may even result in fracturing fluid seepage that pollutes groundwater, posing safety and environmental concerns (Luo et al., 2024). Furthermore, the presence of weak interlayer surfaces adds complexity to the three-dimensional morphology of hydraulic fractures, significantly affecting the evaluation and optimization of fracturing performance (Ouchi et al., 2017). Therefore, it is necessary to conduct in-depth studies of the initiation and propagation behavior of hydraulic fractures under the conditions of interbedded reservoirs

In recent years, hydraulic fracturing of interbedded oil and gas reservoirs has attracted widespread attention. In terms of numerical simulation, researchers have developed various numerical models to simulate fracture propagation behavior and the evolution of complex fracture (Tang et al., 2024; Wang et al., 2025). Research results indicate that geological factors, represented by in-

E-mail address: zhuhaiyan040129@163.com (H.-Y. Zhu).

^{*} Corresponding author.

situ stress, bedding planes, rock mechanical properties, and interlayer interface mechanical properties (Ouchi et al., 2017; Dong et al., 2021; Zeng et al., 2023; Liao et al., 2024; Deng et al., 2024) and as well as engineering factors, represented by pump rate, fluid viscosity, and fracturing technology (Ma et al., 2017; Yu et al., 2022; Huang et al., 2022; Wang et al., 2024; Luo et al., 2024), all have varying degrees of influence on the geometry of HF in interbedded reservoirs. On this basis, researchers have further studied the coupled effects of geological and engineering parameters on fracture propagation. Ou and Liang (2023) proposed through a threedimensional propagation model of fractures in thin interbedded reservoirs that, due to variations in geological parameters, different wells require different settings of fracturing fluid displacement and viscosity. They also found that the greater the cluster spacing or insitu stress difference, the smaller the interlayer thickness required to control fracture height. Gao et al. (2020) studied fracture propagation in interbedded reservoir models under stratified hydraulic fracturing conditions, and the results showed that both reservoir depth and injection rate jointly influence the length, width, and propagation pressure of HFs. Although numerical simulation has provided theoretical support for studying the hydraulic fracturing process in complex reservoirs, most existing studies have focused on the modeling of fracture geometry. Moreover, some simplifying assumptions in the models, such as the fracture surface always maintains a constant internal fluid pressure, have not fully reflected the actual fluid behavior within interbedded reservoirs during hydraulic fracturing operations. This simplification leads to significant discrepancies between the simulated results and the actual fracture propagation, fluid distribution, and conductivity observed in the field, thereby limiting the application value of these simulations in practical engineering (Zhao et al., 2023).

Lab-scale physical simulation experiments are an effective means of studying the mechanisms of hydraulic fracturing. Through systematic physical simulation experimentation, investigators have achieved significant advancements in understanding hydraulic fracture propagation mechanisms within interbedded geological formations (Yang et al., 2023). A large number of scholars believe that the state of in-situ stress is the dominant factor influencing fracture propagation: the smaller the vertical stress, the more pronounced the tendency for the main fracture to propagate along the bedding plane; conversely, the larger the vertical stress, the more likely the main fracture is to penetrate through the bedding plane and propagate along its original direction (Qian et al., 2020; Fu et al., 2022; Guo et al., 2023; Wang et al., 2024). When the horizontal stress difference is large, simple vertical fractures form within the experimental rock samples; otherwise, complex horizontal fractures form. However, when the horizontal stress difference coefficient falls below a threshold, fracture propagation mode shifts to being controlled by weak interlayer surfaces (Jiang et al., 2016; Yu et al., 2022; Ren et al., 2024). Moreover, the mechanical properties of weak interlayer surfaces affect HF propagation patterns, such as propagation along weak discontinuities or being intercepted (Jiang et al., 2016; Lu et al., 2022; Zhai et al., 2023). Bedding planes alter the preferential path of HF originally driven by stress, forming relatively simple fractures due to their low strength (Zhang et al., 2023). The weaker the tensile strength of the bedding, the more readily the primary fracture propagates along the bedding; when the tensile strength is close to that of the matrix, the fracture tends to penetrate the bedding and propagate in its original direction (Sun et al., 2016, 2020). The greater the interlayer thickness and fracture strength, the higher the breakdown pressure, making it more difficult for HF to penetrate the interlayer and more likely to divert along the bedding plane, leading to poor fracturing performance (Zhao et al., 2016). The presence of weak interlayer discontinuities leads to complex fracture propagation, such as fracture path wandering, branching, and shear slip along unbonded interfaces during hydraulic fracturing (Athavale and Miskimins, 2008; Guo et al., 2025). Based on these findings, Hou et al. (2014) conducted multifactor experimental studies of interbedded shale and discovered that under conditions of smaller horizontal stress differences, the complexity of fracture morphology is inversely proportional to the distance between bedding planes. Building upon the above findings, Zhang et al. (2021) concluded that, in interbedded reservoirs using a single fracturing fluid system, the hydraulic fracture geometries mainly include rectangular, elliptical, H-shaped, and gridshaped configurations. Hou et al. (2019) employed an alternating construction scheme of slickwater and guar gum, and observed four typical complex fracture patterns, namely cross-shaped, fishbone-shaped, ladder-shaped, and comb-shaped fracture systems.

Currently, although experimental studies of hydraulic fracturing of interbedded oil and gas reservoirs have made some progress, key challenges remain in achieving comprehensive understanding. On the one hand, most of the existing research focuses on the surface phenomena observed after the fracturing of interbedded rocks, with relatively limited real-time monitoring and evaluation methods, making it challenging to fully capture the dynamic evolution of fractures. On the other hand, most experimental results are based on conditions with 2–3 interbeds of different lithologies. While these experiments simulate the production layers sandwiched between barrier layers, they do not fully reflect the complex growth patterns of HFs within interbedded rocks. Due to the influence of weak interlayer surfaces, the initiation and propagation processes of HF are highly complex, and relying solely on the observation of pump pressure changes and fracture morphology is insufficient to obtain comprehensive information about fracturerelated behavior. Therefore, it is urgent to integrate multiple monitoring methods to interpret the propagation mechanisms of HF in multilayer interbedded rocks from multiple dimensions.

In this study, hydraulic fracturing physical simulation experiments were conducted using synthetic rock samples composed of seven cemented layers under true triaxial stress conditions. The experiments systematically explored the effects of fracturing fluid viscosity, injection rate, and alternating fracturing techniques. By integrating real-time pump pressure monitoring with multichannel acoustic emission (AE) monitoring technology, we comprehensively analyzed the spatiotemporal evolution characteristics of fracture initiation and propagation. Additionally, we thoroughly investigated the mechanical mechanisms underlying fracture propagation through interbedded layers. The findings of this study are expected to provide valuable theoretical support for the efficient extraction of shale oil and gas.

2. Experimental equipment

Based on the independently developed lab-scale true triaxial hydraulic fracturing physical simulation test system, physical simulation experiments on hydraulic fracturing of interbedded reservoirs were conducted. This system primarily consists of a multi-physical field simulation central control console, a true triaxial pressure chamber, a triaxial servo loading system, and an injection system. The physical diagram and flowchart are detailed in Fig. 1. The true triaxial pressure chamber can accommodate cubic rock samples with maximum dimensions of 400 mm \times 400 mm \times 400 mm. The triaxial servo loading system can apply a maximum stress of 50 MPa, while the injection system can provide a maximum injection pressure of 100 MPa.

In addition to this system, the DS5-32C AE monitoring system was utilized to monitor low-energy events caused by local rock failure in real-time. Sixteen sensors, with a stable frequency

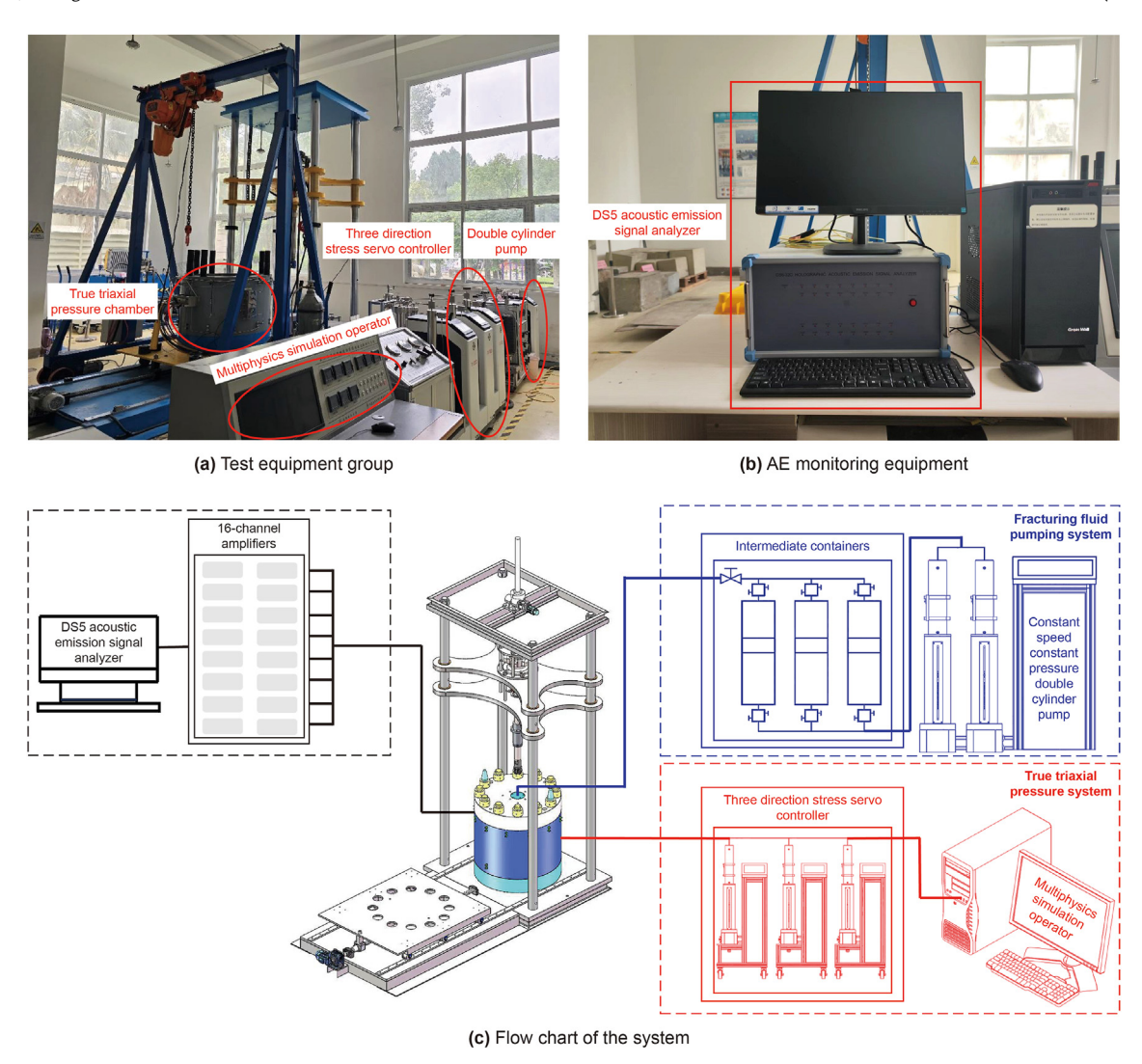


Fig. 1. Lab-scale true triaxial hydraulic fracturing physical simulation test system (Zhao et al., 2024).

response range of 50–400 kHz, were evenly distributed on the four horizontal pressure plates inside the pressure chamber. All preamplifiers were set to amplify signals by 40 dB. The main unit collected and stored full-waveform data at a sampling rate of 3 MB/s per channel.

3. Sample preparation

This study selected the WZ11 oilfield in the Beibu Gulf Basin, located in the western South China Sea, as the research object, which has typical representative characteristics of a complex shale-sandstone interbedded reservoir. First, silicate cement and quartz sand were used as materials, and the mechanical properties of shale and sandstone were simulated by adjusting the proportion of each component to prepare multiple sets of cylindrical cores with a diameter of 25 mm and a height of 50 mm for basic mechanical parameter testing. Then, the formulation whose stress—strain curve most closely resembled that of the real core was selected as the basis for casting the 400 mm cubic fracturing samples in the next step. Ultimately, the mass proportions of each component in the selected artificial rock sample formula are detailed in Table 1, and the measured mechanical and physical properties of the synthetic core samples are summarized in Table 2.

Cement slurry was prepared according to the corresponding formulations, and a layered casting sequence of "sandstone-shalesandstone" was adopted from bottom to top to simulate the vertical heterogeneity of a sandstone reservoir under real conditions. The simulated wellbore was fixed at the center of the top plate of the steel mold. The simulated wellbore had an outer diameter of 16 mm, a wall thickness of 5 mm, and a height of 360 mm, and it was made of 316L alloy steel. Four perforation clusters, each spaced at 90° intervals, were positioned at an elevation of 200 mm from the top plate. Each layer of cement slurry was left to set for 4 h before the next layer was cast to create weak interlayer surfaces. The thickness of the Layers 1 and 7 was 50 mm, while the thickness of Layers 2–6 was 60 mm. After casting was completed and the rock samples reached the designed strength at 28 days, samples containing weak interlayer surfaces were drilled from the rock samples perpendicular to the wellbore direction for interlayer bonding strength testing, and the stress loading direction of each group of experiments was parallel to the weak interlayer surfaces (Fig. 2). The Brazilian disc specimen was 50 mm in diameter and 25 mm in thickness, and the average tensile strength of the weak interlayer surface measured was 2.12 MPa; the size of the direct shear specimen was 50 mm \times 50 mm \times 50 mm, and the average shear strength measured was 4.87 MPa.

Table 1 Synthetic rock sample formulas.

Rock sample	e Composition, %						
	PC42.5 cement	PC52.5 cement	40-mesh quartz sand	60-mesh quartz sand	80-mesh quartz sand	150-mesh quartz sand	Water
Artificial shale	21	21	16	12	6	8	16
Artificial sandstone	_	42	6	8	10	18	16

Table 2 Parameters of synthetic rock cores.

Rock sample	Uniaxial compressive strength, MPa	Elastic modulus, GPa	Poisson's ratio	Fracture toughness, MPa \cdot m $^{1/2}$	Permeability, mD	Porosity, %
Artificial shale	37.26	6.82	0.19	0.27	0.36	17.42
Artificial sandstone	44.48	12.64	0.23	0.30	0.24	16.63

4. Experimental design

4.1. Similarity analysis for the baseline group

4.1.1. Stress condition scaling

In well WZ11-2-x at a depth of 3253 m, the overburden pressure is 71.14 MPa, with a maximum horizontal stress of 68.31 MPa and a minimum horizontal stress of 67.35 MPa. To achieve a stress level similar to in-situ conditions, the scaled-down stress applied in the laboratory experiment was calculated according to Eq. (1). The shape factor must be kept equal to in-situ stress, meaning that the ratio of differences between principal stress components must remain unchanged (Madyarov et al., 2021).

$$R = \left(\sigma_{\mathsf{H}}' - \sigma_{\mathsf{h}}'\right) / \left(\sigma_{\mathsf{v}}' - \sigma_{\mathsf{h}}'\right) \tag{1}$$

where R is the shape factor; σ'_H is the effective horizontal maximum stress, MPa; σ'_h is the effective horizontal minimum stress, MPa; and σ'_v is the effective vertical stress MPa. Since this study uses synthetic rock samples without applied pore pressure, the total stress and effective stress are equal in the indoor experimental scale during the calculation of the similar geological stress, as

detailed in Table 3.

4.1.2. Viscosity and injection rate scaling

In well WZ11-2-x, the lithology at the flow section is primarily shale interbedded with sandstone, where the shale layers develop as good reservoirs. The mechanical and physical parameters measured from the core taken in the well depth range of 3253.83–3259.87 m are shown in Table 4.

In this study, by identifying the dimensionless viscosity at the maximum characteristic propagation time for both field and

Table 3 Calculation of stress scaling.

Parameter	Field scale	Laboratory scale
Vertical maximum stress, MPa	71.14	26
Horizontal maximum stress, MPa	68.31	23
Horizontal minimum stress, MPa	67.35	22
Pore pressure, MPa	38.9	0
Effective vertical maximum stress, MPa	32.24	26
Effective horizontal maximum stress, MPa	29.41	23
Effective horizontal minimum stress, MPa	28.45	22
Shape factor	0.25	0.25

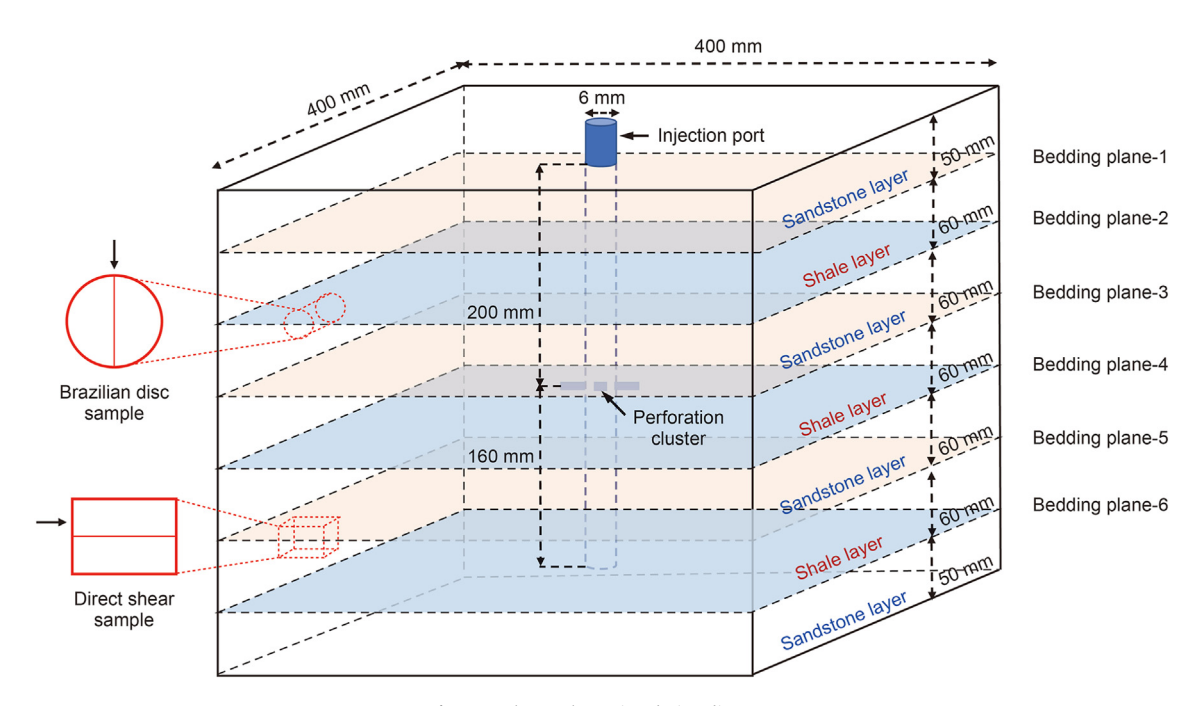


Fig. 2. Rock sample casting design diagram.

laboratory scales, a relationship between the field fracturing fluid viscosity and the laboratory fracturing fluid viscosity was established. The characteristic propagation time can be estimated using an approximate formula concerning the characteristic fracture radius (Bunger et al., 2005). The final simplified formulas for fracturing fluid viscosity and pump speed at laboratory scale are as follows:

$$\mu_l Q_l = \mu_f Q_f \left(\frac{E_f'}{E_l'}\right)^3 \left(\frac{K_l}{K_f}\right)^4 \left(\frac{R'_{lmax}}{R'_{fmax}}\right) \tag{2}$$

where μ is the viscosity, mPa·s; Q is the injection rate, mL/min; E' is the plane strain Young's modulus under ideal radial flow conditions, GPa; K is the fracture toughness, MPa·m^{1/2}; R' is the characteristic radius, m; The subscript l denotes laboratory scale, and f denotes field scale.

In the scaling analysis, the elastic modulus, Poisson's ratio, and fracture toughness were all determined based on the average values obtained from tests of the two rock types. During the experimental process, fracture propagation is constrained by the size of the rock sample; specifically, when a fracture propagates to the boundary of the synthetic rock sample, it can no longer continue to expand. Therefore, the characteristic propagation radius of fractures at the laboratory scale is set at 200 mm. In the field, under conditions of a fracturing fluid viscosity of 3 mPa·s and a pumping rate of 12 m³/min, the characteristic propagation radius of hydraulic fractures is 295 m. To ensure that data are collected over as long a period as possible during the experiment and to avoid rapid dynamic propagation of HFs to the rock sample boundary, the baseline experimental condition is set with an injection rate of 10 mL/min, corresponding to a calculated fracturing fluid viscosity of 33.4 mPa·s.

4.2. Experimental parameters and procedure settings

4.2.1. Experimental parameter settings

The baseline experimental parameters for the physical simulation are as follows for Group #1: Vertical stress 26 MPa, maximum horizontal principal stress 23 MPa, minimum horizontal principal stress 22 MPa, low injection rate 10 mL/min, and medium viscosity 30 mPa·s.

For the other groups, the parameters are adjusted as follows:

Group #2: To evaluate the impact of high-viscosity fracturing fluid and fracturing techniques, medium to high viscosity (30 and 80 mPa·s) fracturing fluids are alternately injected.

Group #3: To assess the effect of varying fracturing fluid viscosities, low to medium viscosity (3 and 30 mPa \cdot s) fracturing fluids are alternately injected.

Group #4: To investigate the influence of injection rate, high injection rate (20 mL/min) fracturing fluid is used.

The four sets of experimental conditions are listed in Table 5.

4.2.2. Experimental procedure

(1) Loading and stress application: Following the creation of notches on two lateral surfaces and the base of the specimen, the prepared rock sample was hoisted into the true triaxial testing system using lifting ropes. The three principal stresses were applied in a stepwise manner: first, the three independent stress loading pumps were set to constant pressure mode to reach the minimum principal stress value; then, the remaining two stress loading pumps were simultaneously increased to the intermediate principal stress level; finally, the vertical stress loading pump was set to the maximum principal stress value. After each stage reached the target stress value, the stress was stabilized for 60 min. The preprocessing of rock samples and AE sensors to be completed beforehand is detailed in Fig. 3(a) and (b).

- (2) Fluid injection setup: Fracturing fluids of different viscosities are introduced into the pumping system. The pumping system is connected to the top of the rock sample using a φ 3 steel injection line and is linked to AE sensors, amplifiers, and receiving terminals, as illustrated in Fig. 3(c).
- (3) Fracturing experiments: For continuous fracturing experiments, no operation is needed for the injection tank. For experiments involving alternating high- and low-viscosity fracturing fluids, when a sudden drop and stabilization of the pump pressure curve is observed, the outlet valve of the high-viscosity fracturing fluid tank is closed, and the outlet valve of the low-viscosity fracturing fluid tank is opened.
- (4) Completion of experiment: The fracturing experiment was considered complete when the injection pressure stabilized at a certain value for more than 300 s or when the fracturing fluid was observed seeping from the surface of the rock sample. After the experiment ended, the rock sample was immediately lifted out. As shown in Fig. 3(d), the rock sample was first disassembled layer by layer in reverse order of casting, using the weak interlayer surfaces as a reference, along a direction perpendicular to the wellbore. Then, the individual layer samples were further disassembled based on the observed fracture conditions. Finally, all cross-sections were reassembled to observe the actual HF morphology and compare it with the AE data.

5. Result and analysis

5.1. Fracture morphology and acoustic emission event localization

To ensure the accuracy of AE event localization results, only events detected by more than six AE sensors were statistically calculated, with a positioning accuracy of 4 mm. We used the AE event locations during the experiment, combined with the reassembled physical cross-sections after the experiment, to study the fracture morphology, propagation trend, and failure mechanism of HF

During the injection of fracturing fluid, due to the

Table 5Four sets of experimental conditions.

Group	$\sigma_{ m V}/\sigma_{ m H}/\sigma_{ m h}$, MPa	Injection rate, mL/min	Viscosity, mPa·s
#1	26/23/22	10	30
#2	26/23/22	10	30/80
#3	26/23/22	10	3/30
#4	26/23/22	20	30

Table 4 Mechanical and physical parameters of rock cores from Well WZ11-2-2 (h = 3253.83 - 3259.87 m).

Lithology	Uniaxial compressive strength, MPa	Elastic modulus, GPa	Poisson's ratio	Fracture toughness, MPa \cdot m ^{1/2}	Permeability, mD	Porosity, %
Shale	52.94	7.26	0.11	0.83	175.8	12.1
Sandstone	76.17	15.36	0.25	0.98	30.9	18.3

incompressibility of the fluid, the pressure in the wellbore quickly increased. This pressure gradually transmitted to the formation around the perforations, and when the stress in this region reached its bearing limit, HF began to initiate. At this point, the elastic energy in the reservoir could be transformed into surface free energy, and fracture propagation was accompanied by plastic energy dissipation and acoustic energy release. Subsequently, HF propagated in the direction perpendicular to the minimum principal stress under the inducement of the maximum and intermediate principal stresses.

Taking the AE localization results of Sample #1 as an example, shown in Fig. 4, black circles represent the spatial locations of AE event points, pink represents the projection on the XZ plane $(\sigma_H - \sigma_V)$, green represents the projection on the YZ plane $(\sigma_H - \sigma_V)$, and blue represents the projection on the XY plane $(\sigma_H - \sigma_V)$, and blue represents the projection on the XY plane $(\sigma_H - \sigma_V)$. We observed that AE events within the rock sample first concentrated around the perforations in the wellbore (Fig. 4(a)), and then gradually spread outward. In addition to vertical propagation, fractures preferentially propagated along the direction of maximum horizontal principal stress and gradually turned, while propagation in the minimum horizontal principal stress direction was inhibited (Fig. 4(b)-(d)).

Furthermore, taking the physical cross-section of Sample #2 as

an example, we found that differences in the mechanical properties of interbeds led to irregular HF propagation in shale-like and sandstone-like layers, deviating from a simple penny-shaped pattern (Fig. 5(a) and (b). The presence of interbed interfaces caused some HFs to be intercepted or horizontally propagated along them, which also resulted in varying degrees of deviation in the main HF plane (Fig. 5(c)). Notably, the rock sample shown in Fig. 5(c) used fracturing fluid containing red and blue tracers (Trace A). The uncolored wetted areas around the HF were caused by the inevitable smearing of Vaseline coupling agent on the AE sensors when removing the rock sample (Trace B).

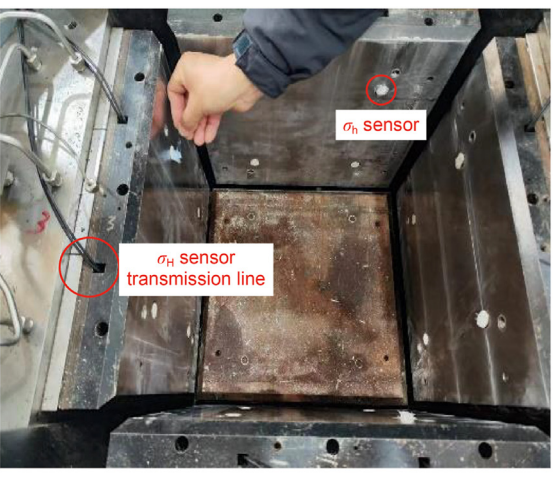
5.1.1. Impact of injection rate (Samples #1 and #4)

Comparing Samples #1 and #4, which serve as control groups, we analyzed the impact of different fracturing fluid injection rates on the vertical penetration and extension of hydraulic fractures. For Sample #4, with an increased injection rate of 10 mL/min compared to Sample #1, the distribution range of AE event points increased by 176 mm in the σ_H direction, 136 mm in the σ_h direction (Figs. 6(a) and 7(a)), and 32 mm in the σ_V direction (Figs. 6(b) and 7(b)).

Moreover, while Sample #1 displayed AE event points concentrating around the wellbore, with a notable concentration at 200 and 1400 s (Fig. 6(a)), Sample #4 showed a scattered distribution of



(a) The cast rock samples are ready for hoisting



(b) Apply coupling agent to AE sensors on triaxial stress plates



(c) Different viscosity fracturing fluids are introduced into corresponding tanks



(d) The cross-sections of the specimens were exposed after the experiment

Fig. 3. Schematic diagram of the experimental process.

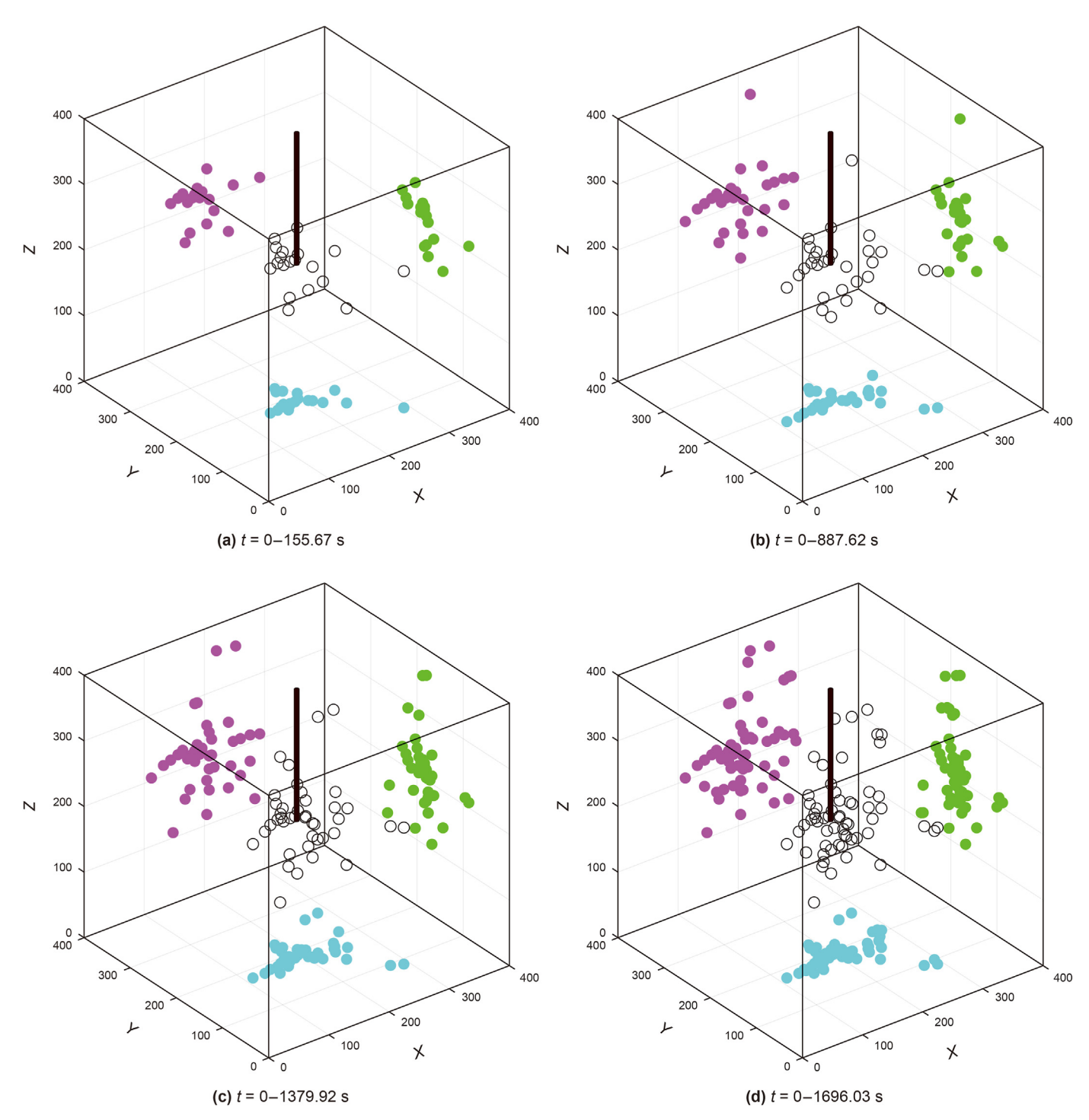


Fig. 4. AE event localization during the experiment for Sample #1.

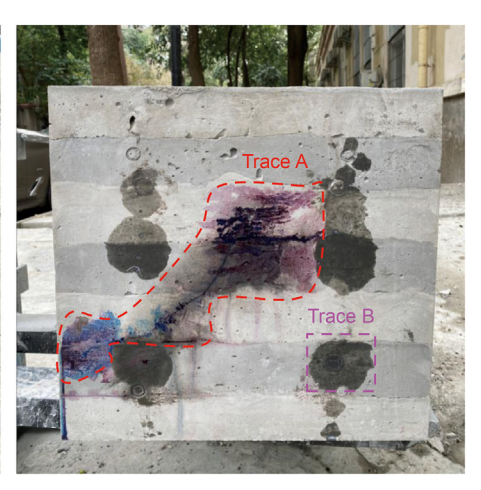
AE event points within the rock sample, expanding extensively towards the boundaries of the sample along the maximum horizontal principal stress direction. This indicates that the HF rapidly extended to the far end near the rock sample's side after initiation (Fig. 7(a)).

The assembled cross-section of the physical rock sample shows that for Sample #1 a vertical main fracture was formed internally, with a vertical propagation range covering 4 layers, and horizontal propagation occurred along the weak interlayer planes at the

2nd—5th layers. The vertical fracture was relatively symmetrical (Fig. 6(c)). For Sample #4, the HF propagated vertically across five layers, with minimal interlayer propagation. Horizontal propagation traces were observed only at the 4th and 5th bedding planes, while the fracture surface exhibited a simpler and more continuous morphological pattern. It is worth noting that, in order to confirm the absence of HF in other layers of Sample #4, the sample was extensively broken down, making it difficult to fully reassemble some of the layers. The final exhibited main HF surface is shown in





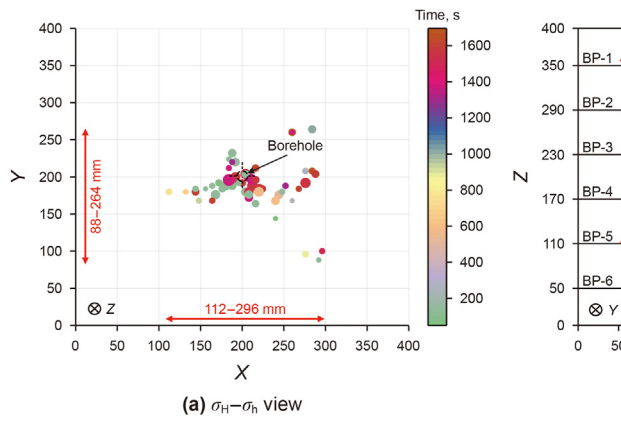


(a) Main view of sandstone-like layer (5th layer)

(b) Main view of shale-like layer (6th layer)

(c) Overall side view

Fig. 5. Fracture morphology after the experiment for Sample #2.



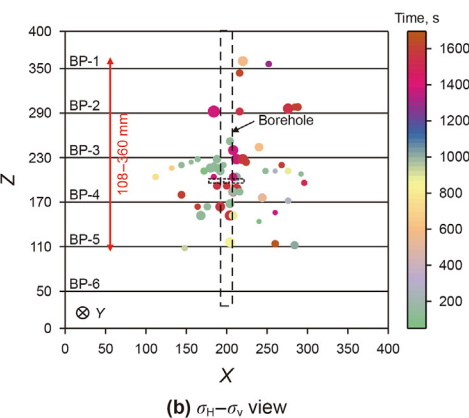
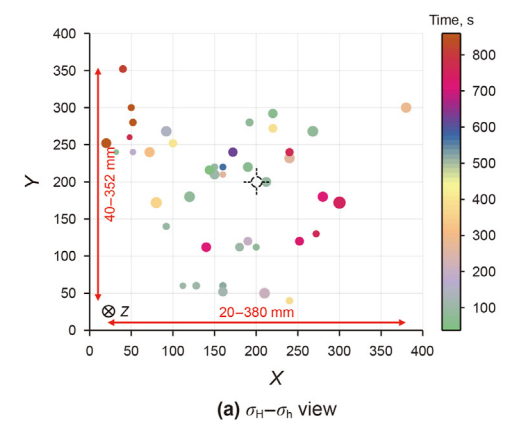
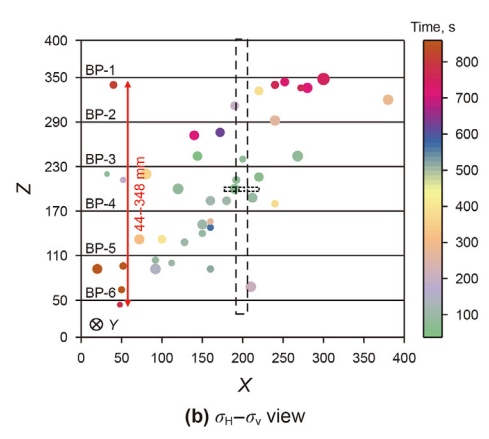




Fig. 6. AE distribution and fracture morphology for Sample #1.





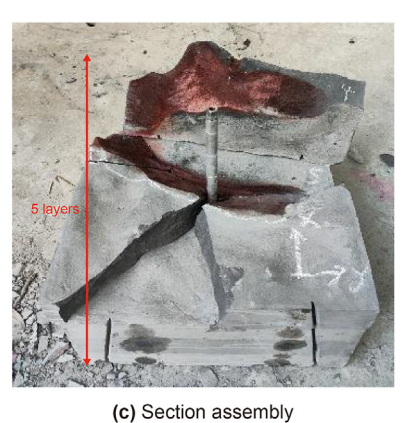


Fig. 7. AE distribution and fracture morphology for Sample #4.

Fig. 7(c).

5.1.2. Impact of viscosity (Samples #2 and #3)

To investigate the effect of fracturing fluid viscosity on the vertical penetration and extension of hydraulic fractures, Sample #1 was kept unchanged, while the construction scheme was altered for Samples #2 and #3. For Sample #2, fracturing fluids with

viscosities of 80 and 30 mPa·s were alternately injected. For Sample #3, the construction scheme was also altered, but the fracturing fluid viscosities were reduced to 30 and 3 mPa·s.

The AE event point distribution ranges for these two experiments were as follows: in the σ_H direction, 52–304 mm for Sample #2 and 40–380 mm for Sample #3, and in the σ_h direction, 100–396 mm for Sample #2 and 24–372 mm for Sample #3

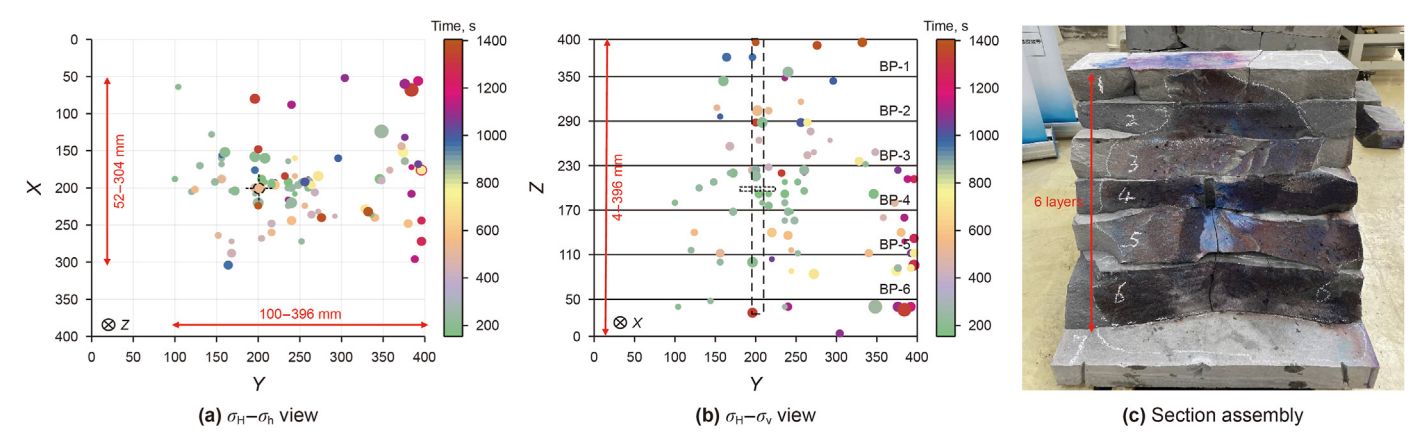


Fig. 8. AE distribution and fracture morphology for Sample #2.

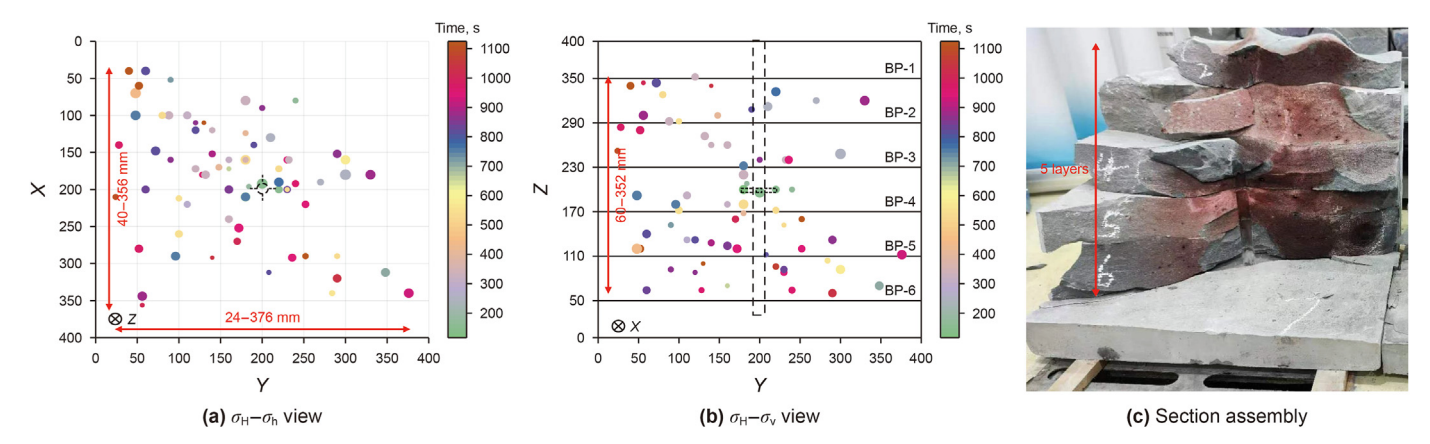


Fig. 9. AE distribution and fracture morphology for Sample #3.

(Figs. 8(a) and 9(a)). In the σ_V direction, the ranges were 4–396 mm for Sample #2 and 60–348 mm for Sample #3 (Figs. 8(b) and 9(b)). The results show that the vertical dimension of the HF in Sample #2 is greater than that in Samples #1 and #3, while the horizontal dimensions in both directions are greater in Sample #3 compared to Samples #1 and #2. For Sample #2, the AE events were highly concentrated around the wellbore within the initial 200 s of fracturing. Over time, these events expanded longitudinally outwards, broke through the weak interlayer planes, and then extended asymmetrically along the direction of the maximum horizontal principal stress until reaching the sample boundary. In contrast, for Sample #3, the AE events were generally detected later with lower energy values. These events gradually accumulated near the weak interlayer planes over time but ultimately failed to penetrate the barriers of the 1st and 6th weak interlayer planes (Fig. 9(b)).

The longitudinal main fracture surface in Sample #2 propagated through 7 layers, with horizontal extensions developing along the weak planes between the 1st and 6th layers. The fracture extended to the horizontal boundaries of the sample at the 4th–6th bedding planes resulting in a larger fracture area. In contrast, Sample #3 exhibited a hydraulic fracture that extended through 5 layers vertically and was intercepted at the 6th bedding plane. Horizontal extension occurred along the weak interlayer planes at the 1st–5th bedding planes. The lower fracture wings of both samples extended relatively vertically along the $\sigma_{\rm V}$ direction, with vertical extension predominantly marked by high-viscosity fracturing fluid (corresponding to blue in Fig. 8(c) and red in Fig. 9(c)). In contrast, horizontal extension along the interbedded interfaces was mainly

characterized by low-viscosity fracturing fluid (corresponding to red in Fig. 8(c) and colorless in Fig. 9(c)).

5.2. Pump pressure response and acoustic emission characteristics

Based on the AE parameter analysis method, microcracks can be categorized into two types: tensile and shear (Ohno and Ohtsu, 2010). According to the JCMS-III B5706 standard, this method requires the use of the ratio of RA to AF as the criterion (Chen et al., 2023). Here, AF is calculated as the number of "ringing counts" divided by the "duration", representing the average frequency of a single AE event. RA is calculated as the "rise time" divided by the "amplitude", indicating the reciprocal of the AE signal waveform gradient in ms/mV. These parameters have high sensitivity and resolution for identifying the initiation and propagation stages of fractures and can provide critical information on the dynamic development of fractures.

$$RA = \frac{Rise time}{Peak amplitude}$$
 (3)

$$AF = \frac{Count}{Duration} \tag{4}$$

where Rise time is the time interval from the initial arrival time to the maximum amplitude, ms; Peak amplitude is the maximum value of the waveform signal, V; Count refers to the number of times the waveform crosses the threshold during a single acoustic

emission hit duration, dimensionless; Duration refers to the time interval from the initial arrival time to when the acoustic emission waveform decays below the threshold value, ms.

Due to the instantaneous release of elastic energy, tensile fractures typically exhibit shorter rise times and durations, while having relatively larger amplitudes and counts, resulting in a low RA and high AF phenomenon. Conversely, shear fractures exhibit the opposite characteristics, with low AF and high RA distributions (Yang et al., 2023). Previous studies have suggested using a linear method to differentiate between the two types of fractures (Ohno and Ohtsu, 2010), finding that it has the advantages of being efficient and versatile. Therefore, this study continues to use the straight-line classification method and employs the K-means clustering algorithm to determine the parameters of the boundary line. From the perspective of micro-seismic energy, the energy release patterns for shear and tensile fractures differ; layer-parallel slip generally results in shear fractures, while breaking through layering results in tensile fractures. Therefore, this study combines the calculated arrival times and energies of acoustic emission events with fracturing fluid pressure and viscosity to investigate the time evolution mechanisms of hydraulic fractures and the responses of different AE characteristic parameters during hydraulic fracturing.

According to the combined analysis of pump pressure curves and AE events, the pressure curves for the four rock samples exhibited varying degrees of unstable fluctuations. This was primarily due to the restricted fracture propagation, characterized by repeated processes of initiation, propagation, energy accumulation, and re-fracturing. The AE events were unevenly distributed within the injection intervals. Specifically, a quiescent period was observed at the beginning of the injection, followed by a concentration of high-energy tensile events around the time of pressure drop, and subsequently, shear events occurred. This behavior is attributed to the constant flow injection mode used in this study, which led to a continuous increase in fluid pressure within the wellbore, creating high-stress zones. The surrounding particles, with varying stiffness, deformed differently, leading to stress concentration and the formation of primary micro-fractures. These micro-fractures coalesced to form hydraulic fractures, resulting in shear fractures. During the subsequent fracture propagation stage, the high-pressure fluid accumulated in the wellbore diffused into HFs and drove their propagation. The fluid pressure exhibits a gradient distribution, with non-uniform pressure levels extending from the injection point to the fracture tip, leading to the generation of both tensile and shear fractures (Zhao et al., 2023). Through statistical analysis of AE events, the following observations were made: the total number of AE events in the experiments ranked as #2 > #3 > #4 > #1, and the proportion of shear AE events ranked as #1 > #3 > #2 > #4.

5.2.1. Effect of injection rate

Compared to Sample #1, Sample #4 was tested with 10 mL/min increased injection rate while other experimental conditions kept unchanged. For Sample #1, the first drop in fracturing pressure occurred at 145 s, with a fracture initiation pressure of 28.2 MPa. During this period, the pressure rise rate was approximately 0.19 MPa/s (Fig. 10(a)). In contrast, Sample #4 achieved an initiation pressure of 33.91 MPa at 79 s, with a pressure rise rate of approximately 0.43 MPa/s, significantly increasing the rate of pressure rise (Fig. 10(d)).

Throughout the experiment, the total AE count in Sample #4 was reduced by 29% compared to Sample #1, while the proportion of tensile events increased by 37%. A total of five high-frequency AE event periods were monitored in Sample #1, all corresponding to pressure drop points in the pump pressure curve, indicating macro-

fracture formation. During the remaining periods, the sample was relatively calm, representing HF propagation and extension. Analysis shows that although Sample #4 had fewer total AE events, it had the highest proportion of tensile events (the maximum among all control groups), with higher energy values for individual tensile AE events. Consequently, the cumulative energy value for Sample #4 was only about 15% lower than that of Sample #1 during the experimental period. This indicates that under high injection rates. the net pressure within the fracture increases, enhancing the fracture propagation capability. This results in a large number of tensile fractures predominantly governed by tensile failure, leading to a pronounced vertical penetration of the HF and a significant reduction in horizontal extension along the bedding planes. However, due to the rapid injection, the HF expands quickly to the sample boundary, leaving insufficient time for the formation of a complex fracture network.

5.2.2. Effect of viscosity

When using high-viscosity fracturing fluids (Fig. 10(b) and (c)), the peak pressure for Sample #2 (80 mPa·s) was essentially the same as that for Sample #3 (30 mPa·s). However, when using low-viscosity fracturing fluid, the fracture propagation pressure of Sample #2 (30 mPa·s) remained stable around 24 MPa, which was significantly higher than the 18 MPa observed for Sample #3 (3 mPa·s). Additionally, the overall experimental curve for Sample #2 exhibited more pronounced sawtooth fluctuations, with post-drop pump pressure values being higher compared to the third group; the viscosity changes in Sample #3 during the fracture propagation phase had almost no effect on the injection pressure, which tended to slowly rise to a nearly horizontal minimum boundary load ($\sigma_h = 22$ MPa).

Throughout the experiment, the total AE count in Sample #2 increased by 32% compared to Sample #3, and the proportion of tensile events rose by 21%. For these two groups of rock samples, during the high-viscosity fracturing fluid stage, the pump pressure increased to a higher level, and a large number of tensile events were detected. The AE energy remained at a high value for a period of time, accompanied by multiple pressure drops. This indicates that micro-fractures within the rock sample continuously accumulate and coalesce into macro-fractures. In contrast, during the low-viscosity fracturing fluid stage, the AE count significantly decreased, and the pump pressure curve extended nearly horizontally, indicating that the internal fractures of the rock samples were expanding under a relatively stable pressure.

5.3. Construction scheme and spatiotemporal evolution characteristics of AE

Compared to homogeneous sandstone reservoirs, the hydraulic fracturing behavior in shale-sandstone interbedded reservoirs differs significantly. The presence of bedding planes between layers has a profound impact on the fracture propagation path, morphology, and final conductivity. Simply relying on a single vertical main fracture for modification is often insufficient to achieve the desired effect; activating the bedding planes to form more branch fractures is necessary. Therefore, investigating the factors influencing bedding plane activation is crucial for promoting efficient hydraulic fracture propagation across multiple interbedded layers, forming complex fracture network systems, and enhancing unconventional gas recovery.

To reveal the impact of different engineering factors on bedding plane activation, this study utilized AE positioning from Section 4.1 and AE classification results from Section 4.2. AE events detected at the bedding planes of Samples #1—#3 were plotted on the pump pressure curves and the σ_H - σ_h horizontal planes for analysis and

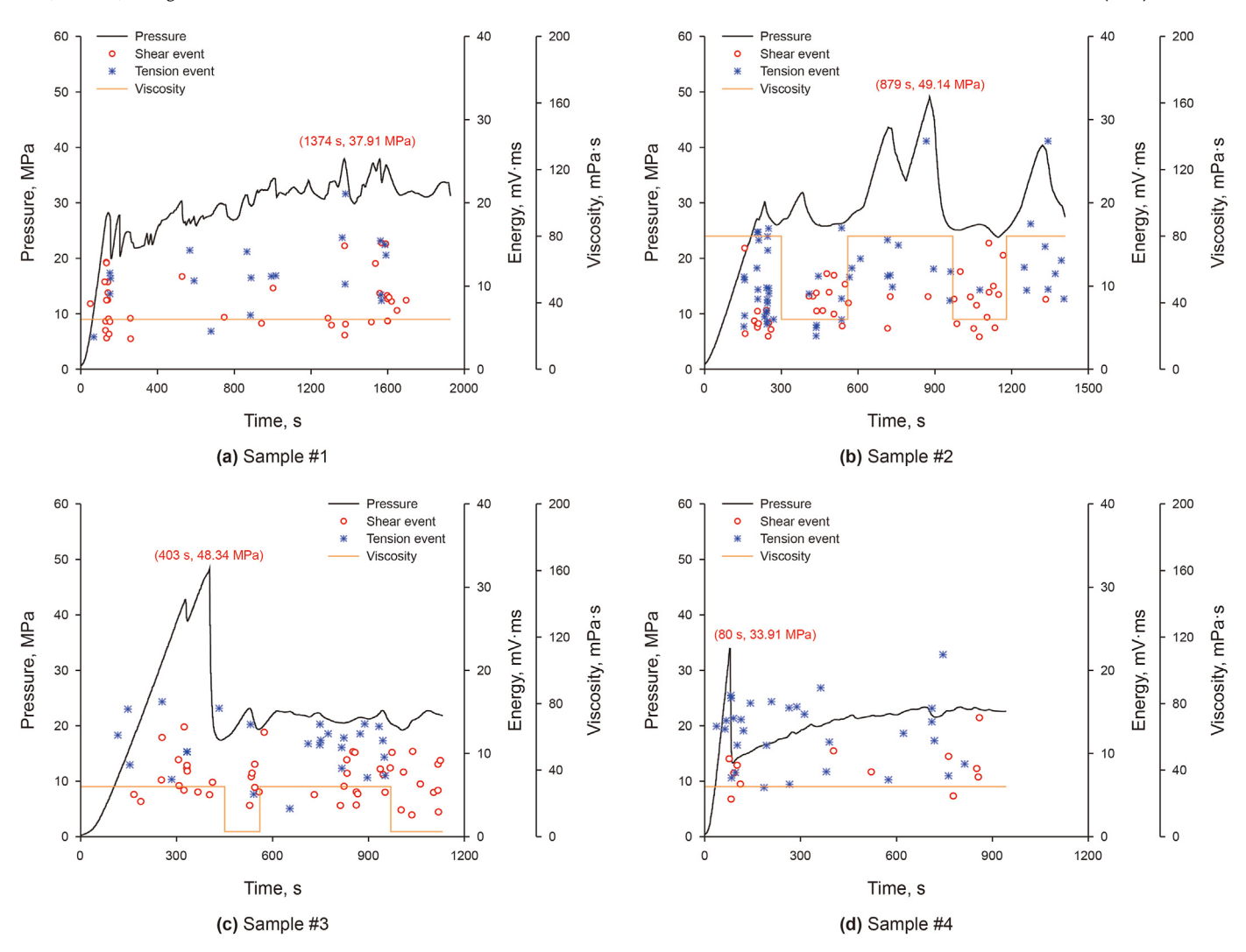


Fig. 10. Joint analysis chart of injection pressure and AE.

compared with the physical top views of each layer.

For Sample #1, following the initial pressure decline at 145 s corresponding to main fracture initiation, notable pressure declines were observed near the 3rd bedding plane at 1363 and 1586 s. The projections on the horizontal plane showed dense distribution of shear events, suggesting that at 1363 s, the fracture underwent secondary vertical extension at the 3rd bedding plane, and at 1586 s, it not only extended vertically but also opened the bedding plane horizontally (Fig. 11(a)). Similarly, shear-dominated AE events were predominantly detected at the 4th bedding plane at 1586 s, suggesting that the HF simultaneously opened part of the bedding plane at this location (Fig. 11(b)). At the 2nd bedding plane, shear-dominated AE events were detected at 1600 s, indicating that the HF had opened fewer bedding planes near the main fracture face at this time (Fig. 11(c)). Tensile AE events were detected at the 5th bedding plane at 863 s, followed exclusively by shear events, indicating that the HF had extended to the 5th bedding plane and was intercepted. Subsequently, the HF switched to horizontal extension, opening the bedding plane (Fig. 11(d)). Notably, the absence of AE events near the 1st bedding plane suggests insufficient energy for fracture penetration through this structural discontinuity (Fig. 11(e)).

For Sample #2, the main fracture was initially observed to develop in Layer 4, subsequently propagating bidirectionally

toward the 3rd and 4th bedding planes. During the high-viscosity fracturing phase (80 mPa \cdot s), tensile events were detected at the 3rd bedding plane at 732 and 884 s, corresponding to secondary and tertiary vertical extensions of HF that increased the main fracture surface area and extended its intersection lines with the bedding planes (Fig. 12(a)). During the subsequent medium viscosity fracturing phase (30 mPa \cdot s), two shear-type AE events were detected around 530 s, suggesting that the HF expanded horizontally along the bedding plane. At the 4th bedding plane, two shear-type AE events were recorded around 580 s, indicating that the HF opened part of the bedding plane (Fig. 12(b)). Continued monitoring during medium-viscosity fracturing revealed shear-type AE events at the 1st, 2nd, 5th, and 6th bedding planes between 900 and 1200 s, and at the 3rd and 5th bedding planes from 530 to 600 s (Fig. 12(c)—(f)).

For Sample #3, tensile AE events were detected at the 3rd bedding plane at 720 and 936 s during the medium-viscosity fracturing phase (30 mPa·s), indicating secondary and tertiary vertical extensions of the HF (Fig. 13(a)). At the 4th bedding plane, shear-dominated AE events were observed at 582 s during the low-viscosity fracturing phase (3 mPa·s), indicating horizontal extension of the HF and opening of some bedding planes (Fig. 13(b)). According to Fig. 13(c) and (d), tensile AE events were recorded at the 2nd and 5th bedding planes at 870 s (medium-viscosity

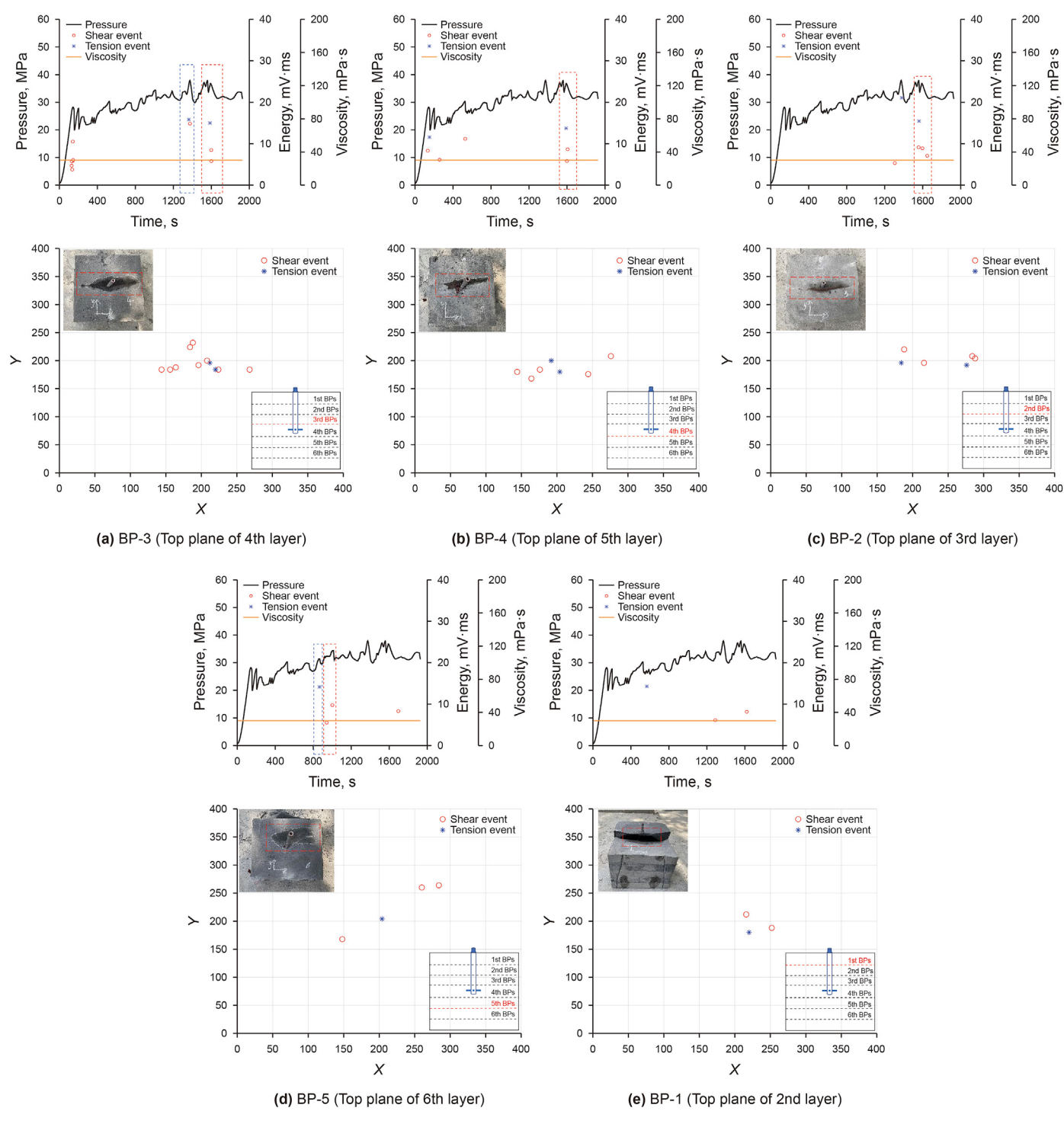
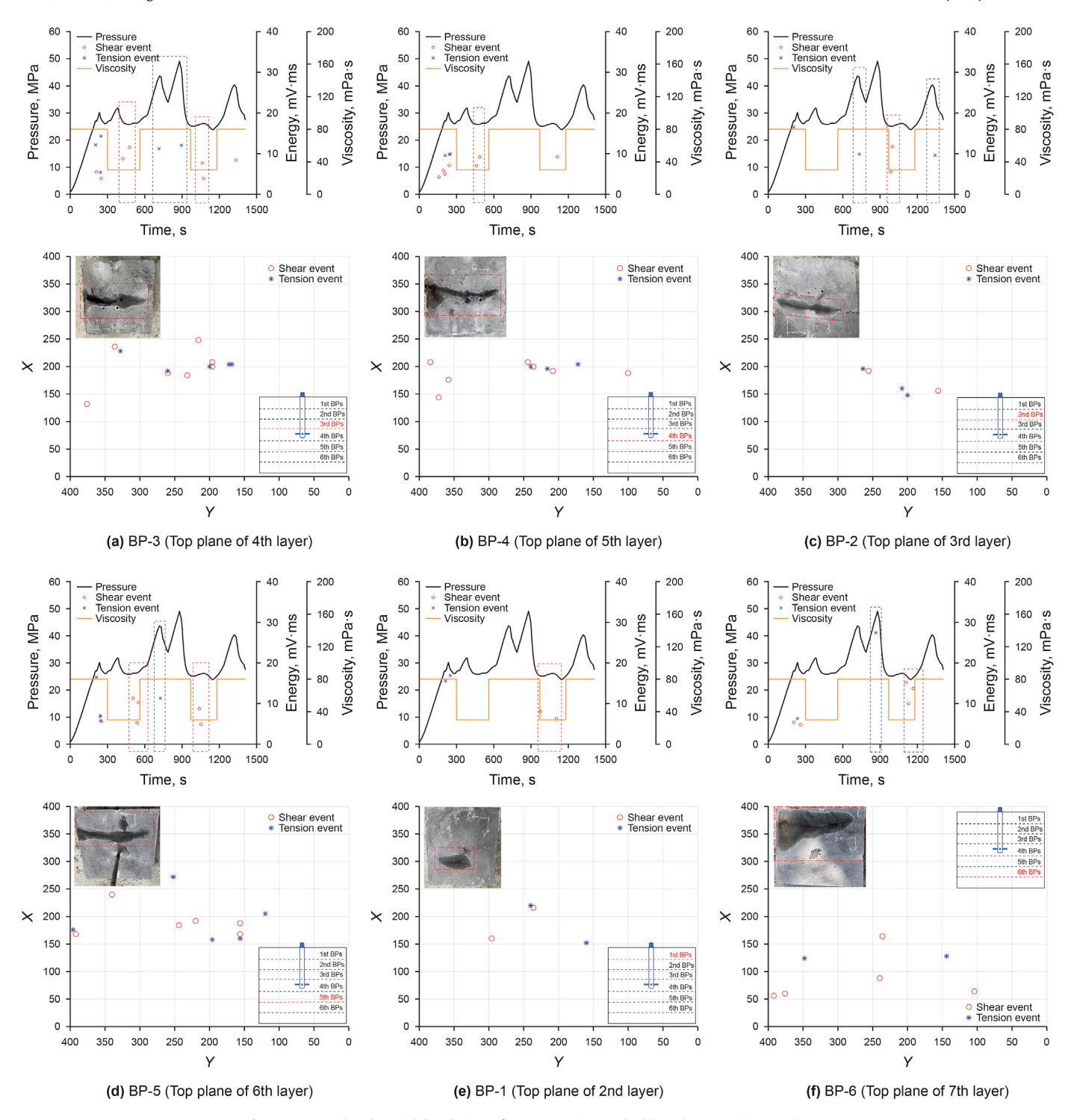


Fig. 11. Temporal and spatial distribution of AE event points on bedding planes 1-5 in Sample #1.

fracturing fluid stage), while shear AE events were observed at 930 s (end of this stage). The physical cross-section reveals that the main fracture trace at the 2nd bedding plane is closer to the sample boundary, suggesting that the HF experienced asymmetric propagation influenced by interbedding interfaces, with differing extension rates on either side of the vertical direction. Shear-dominated AE events were detected at the 1st bedding plane between 900 and 1200 s (Fig. 13(e)), signifying horizontal HF propagation that ultimately extended beyond the sample boundary.

Generally, shear-type AE events exhibited higher occurrence frequencies near weak interlayer surfaces during lower-viscosity fracturing fluid injection stages, with satisfactory spatial correlation between AE event localization and actual fracture morphology. 4 bedding planes (BP-2 to BP-5) were activated in Sample #1, while 5 (BP-1 to BP-5) and 6 (BP-1 to BP-6) bedding planes were respectively activated in Samples #3 and #2.

This phenomenon can be attributed to the continuous injection scheme employed in Sample #1, where a medium-viscosity fracturing fluid (30 mPa·s) was maintained without viscosity modification. The sustained fracture propagation under this condition caused progressive dissipation of fluid energy within the fractures, leading to inadequate weak interlayer plane activation. For Sample

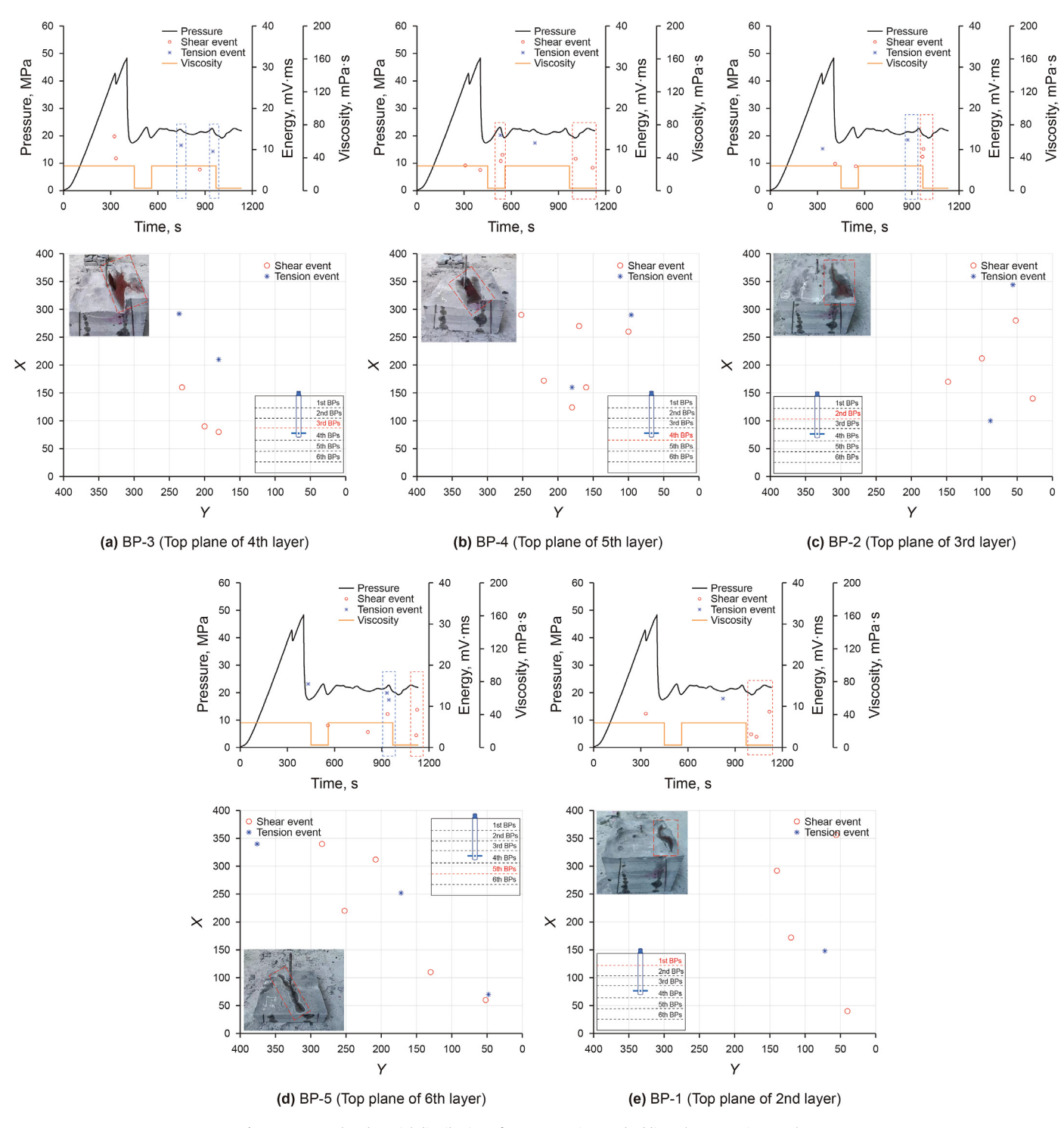


 $\textbf{Fig. 12.} \ \ \textbf{Temporal and spatial distribution of AE event points on bedding planes 1-6 in Sample ~\#2.}$

#3 subjected to alternating-viscosity injection sequences, although medium-viscosity fluid was initially employed during the pre-fracturing stage with limited vertical layer connectivity, subsequent lower-viscosity fluid injection (3 mPa·s) enhanced weak interlayer plane activation and horizontal fracture development compared to Sample #1.

In Sample #2, a high-viscosity fracturing fluid (80 mPa·s) was injected, which resulted in lower fluid loss along the weak

interlayer surfaces. After reaching the lithological interface, the relatively concentrated hydraulic energy ensured that the HF could penetrate and connect multiple weak interlayer surfaces. This provided the prerequisite conditions for the subsequent activation of all weak interlayer planes and varying degrees of horizontal propagation during the subsequent low-viscosity fracturing fluid stage, ultimately yielding the most favorable stimulation efficacy among the tested samples.



 $\textbf{Fig. 13.} \ \ \text{Temporal and spatial distribution of AE event points on bedding planes 1-5 in Sample $\#2$.}$

6. Discussion

The HF propagation mechanism is intrinsically correlated with rock mechanical parameters, the fluid pressure distribution within the fracture, and the stress concentration at the fracture front. Analysis of the stress intensity factor (SIF) at the fracture tip provides critical insights into the physical processes governing fracture propagation under weak interlayer planes influence. Warpinski and Teufel. (1987) hypothesized that the fracture tip temporarily

becomes blunted when it contacts a discontinuity. Specifically, when an HF propagates to a weak interlayer planes, it can only cross, activate, or propagate along the bedding plane after a certain period of injection.

According to fracture mechanics theory, the HF at this stage can be simplified and analyzed as a symmetrical fracture with a half-length of a. Fracture propagation initiates when the Mode I SIF ($K_{\rm I}$) reaches the fracture toughness ($K_{\rm IC}$) of the rock matrix. Owing to fluid lag effects, there are two possible force conditions on the

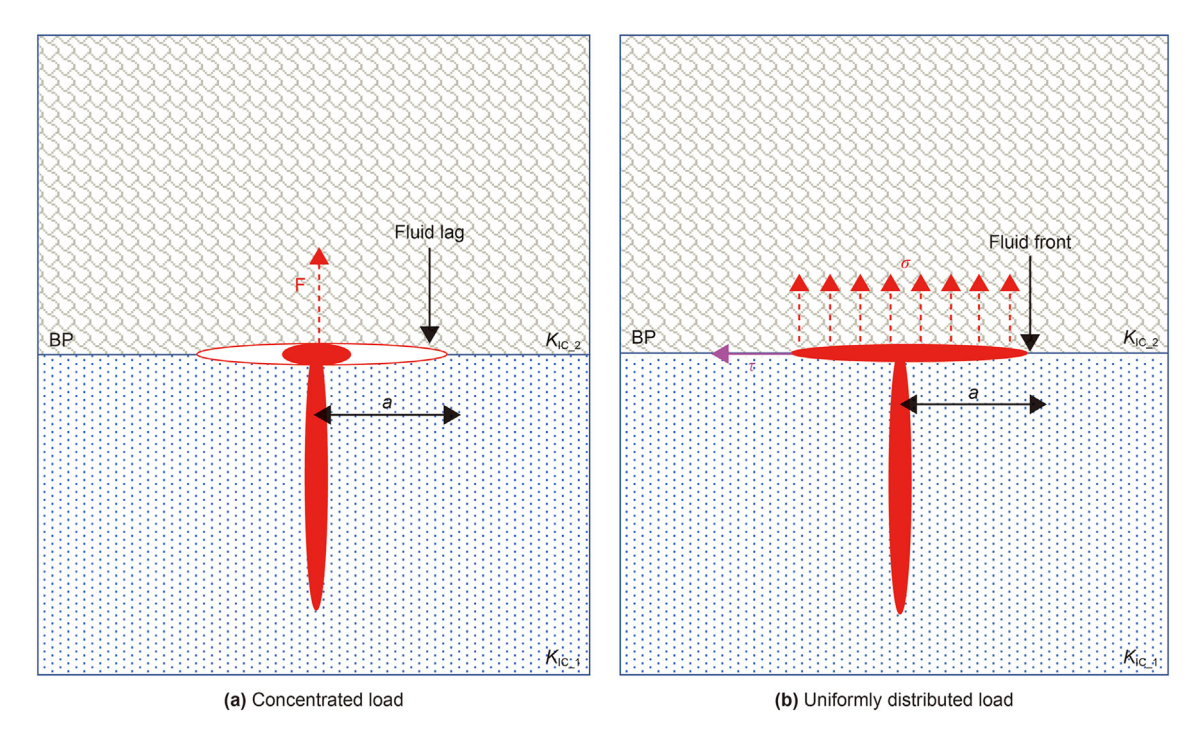


Fig. 14. Schematic diagram of the loading mode after HF intersects with the weak interlayer plane (modified from Wu et al., 2022).

fracture surface: when significant fluid lag develops with central fluid accumulation, the fracture surface experiences quasiconcentrated loading (Fig. 14(a)). Conversely, when fluid penetration approaches the fracture tip and the fracture is almost fully filled with fluid, the fracture surface is approximately subjected to a uniformly distributed load (Fig. 14(b)).

$$K_{\rm I1} = \frac{F}{\sqrt{\pi a}} \tag{5}$$

$$K_{12} = \sigma \sqrt{\pi a} \tag{6}$$

$$\tau - \lambda(\sigma_{\rm n} - P) = 0 \tag{7}$$

where K_{11} and K_{12} are the SIFs, MPa·m^{1/2}; a is the half-length of the fracture, m; F is the equivalent concentrated stress, MPa; σ is the equivalent uniformly distributed stress, MPa; τ is the shear stress at the fracture tip, MPa; σ _n is the normal stress applied to the weak interlayer planes, MPa; λ is the friction coefficient of the weak interlayer planes; P is the fluid pressure, MPa.

High-viscosity fracturing fluid, due to its poor mobility, easily forms a fluid lag region. In this scenario, it corresponds to a concentrated load at a single point. According to Eq. (5), the reduced SIF at the fracture tip under such conditions decelerates fracture propagation along bedding planes, promoting hydraulic energy accumulation within the HF. When the $K_{\rm I}$ at the center of the HF exceeds $K_{\rm IC}$ of the matrix on the other side of the weak interlayer plane, Mode I tensile failure occurs, causing the HF to propagate perpendicularly through the layer, breaking through the interlayer barrier.

In contrast, low-viscosity fracturing fluid has better flowability, which allows the fracture to be as fully filled with fluid as possible. This corresponds to uniformly distributed loading along the fracture surface. According to Eq. (6) the degree of stress concentration at the fracture tip is higher in this case, which means that even with a small variation in net pressure within the fracture, the HF tends to

continuously propagate along the weak interlayer planes without accumulating hydraulic energy. Moreover, low-viscosity fracturing fluid is more likely to filtrate into the weak interlayer plane, reducing the maximum static friction force exerted on the weak interlayer plane. According to Eq. (7), when the shear stress meets the Mohr—Coulomb criterion, shear sliding occurs along the weak interlayer plane, driving the HF to activate the weak interlayer plane and extend horizontally. At the same time, the flow characteristics of low-viscosity fracturing fluid effectively reduce the fluid lag effect within the HF, establishing a more unobstructed pathway for fluid flow inside the fracture. This creates favorable conditions for subsequent high-viscosity fluid injections, allowing for higher stress to be applied at the fracture tip and further enhancing the effect of through-layer propagation.

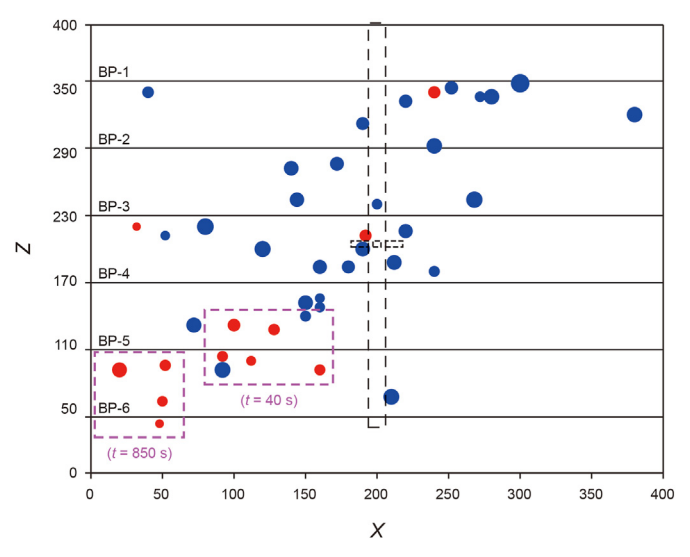


Fig. 15. Overall AE event point distribution of Sample #4.

This explains well the experimental phenomena observed in this study. Specifically, high-viscosity fracturing fluid is more conducive to through-layer propagation of the HF, corresponding to the concentration of high-energy tensile AE events observed during the drop in pump pressure; low-viscosity fracturing fluid is better at opening weak interlayer planes between layers, corresponding to shear AE events occurring near the spatial location of the weak interlayer plane; alternating injections of high- and low-viscosity fracturing fluids increase the complexity of the fracture network, corresponding to mixed tensile-shear AE events being observed in a spatiotemporal sequence.

For a high injection rate, since the net pressure within the fracture can be increased and replenished in a timely manner, the fracture tip can be rapidly filled with fluid. Theoretically, this promotes the HF to cross the weak interlayer planes and expand along it, increasing the complexity of the fracture network. However, due to the influence of the laboratory-scale experiment, it was observed that HF in Sample #4 may have exhibited dynamic propagation, which could negate any contribution of fluid pressure to the new fracture surfaces (De Pater et al., 1994), resulting in differences between the experimental results and field conclusions. Specifically, shear-type AE events were only sporadically distributed near the weak interlayer plane between the 5th layer during the early and late stages of the experiment, and the experiment ended significantly earlier than expected (Fig. 15). Additionally, the physical cross-section exhibited a simple fracture morphology with almost no opening of weak interlayer planes or formation of branch fractures (see Fig. 7(c)). It is speculated that under these conditions, the high injection rate caused the HF to undergo unstable, uncontrolled, and rapid propagation, thereby reducing the volume and complexity of the fracture network. On the field scale, using a high injection rate in conjunction with a high-viscosity fracturing fluid could result in extremely high treatment pressures, potentially exceeding the pressure limit and causing pump shutdown, which is generally not adopted.

Therefore, in this study, an alternative condition (Sample #2) was set up as a control group, using alternating injections of a higher viscosity fracturing fluid instead of increasing the injection rate. The findings showed that this also enhanced the through-layer propagation of HF. This indicates that the interaction behavior of HF with weak interlayer surfaces in interbedded rock samples is related to the product of fluid viscosity and injection rate. When the product of fluid viscosity and injection rate is similar under other constant conditions, it may lead to similar interaction behavior between HF and weak interlayer surfaces, and similar phenomena have also been observed in previous studies (Tan et al., 2017).

7. Conclusions

In this study, large-sized synthetic rock samples were used to conduct HF physical simulation experiments under the guidance of similar material scaling theory. By setting up 6 composite weak interlayer planes, and ensuring consistency of geometric and mechanical properties between layers and weak planes based on standardized sample preparation procedures, the experiment focused on studying the initiation, propagation, morphology, and underlying mechanisms of HF in interbedded reservoirs with multiple discontinuities, under the influence of engineering factors such as injection rate, fluid viscosity, and construction scheme. The main conclusions are as follows.

(1) During the hydraulic fracturing physical simulation process, AE with high temporal and spatial resolution, combined with real-time pump pressure recording, is able to capture the dynamic process of HF formation and propagation. There is a

strong correlation between the spatial distribution of AE events and the actual morphology of the fractures. The mechanical mechanism is that the onset and propagation of microcracks are closely related to the tensile and shear fracture properties. Tensile-type AE events represent the formation of the main fracture and its vertical through-layer propagation, while shear-type AE events indicate the activation of weak interlayer surfaces and the trend of fracture propagation along these weak interlayer planes. The number of layers connected by HF and the extent of weak plane activation determine the formation of a complex fracture network.

- (2) High-viscosity fracturing fluid effectively increases the injection pressure, promoting the vertical through-layer propagation of the main fracture. In contrast, low-viscosity fracturing fluid is more easily captured by the weak interlayer planes, tending to activate weak interlayer planes and promoting horizontal propagation of the fracture, forming branch fractures. Although increasing the injection rate can enhance the vertical propagation of fractures, it also causes deviation of the main fracture plane, weakening the ability to activate horizontal bedding planes, which results in a relatively simple fracture network morphology.
- (3) The alternating injection of fracturing fluids with different viscosities enables the main fracture to break through height limitations while promoting the full development of branch fractures along weak interlayer planes. This ultimately forms a complex fracture network and achieves effective threedimensional reservoir modification.

CRediT authorship contribution statement

Chao Liu: Writing — original draft, Software, Conceptualization. **Hai-Yan Zhu:** Writing — review & editing, Validation, Supervision, Funding acquisition. **Kai Tang:** Writing — review & editing. **Peng Zhao:** Writing — review & editing, Validation, Supervision. **Xuan-He Tang:** Funding acquisition. **Lei Tao:** Funding acquisition, Data curation. **Zhao-Peng Zhang:** Funding acquisition. **Guo-Hui Ren:** Writing — review & editing.

Declaration of competing interest

All of authors declare that they have no conflict of interest.

Acknowledgements

This study was financially supported by the National Key Research and Development Program of China (Grant Nos. 2023YFF0614102 and 2023YFE0110900), the National Natural Science Foundation of China (Grant Nos. 52374004, 52204005, and 52304003), and the Natural Science Foundation of Sichuan Province (Grant Nos. 2024NSFSC0961 and 2023NSFSC0940).

References

Athavale, A., Miskimins, J., 2008. Laboratory hydraulic fracturing tests on small homogeneous and laminated blocks. In: 42nd US Rock Mechanics Symposium and 2nd U.S.-Canada Rock Mechanics Symposium.

Bunger, A., Jeffrey, R., Detournay, E., 2005. Application of scaling laws to laboratoryscale hydraulic fractures. In: 40th U.S. Symposium on Rock Mechanics (USRMS), ARMA-05-818. American Rock Mechanics Association.

Chen, Z., Zhang, G., He, R., et al., 2023. Acoustic emission analysis of crack type identification of corroded concrete columns under eccentric loading: a comparative analysis of RA-AF method and Gaussian mixture model. Case Stud. Constr. Mater. 18, e02021. https://doi.org/10.1016/j.cscm.2023.e02021.

Deng, Y., Xia, Y., Wang, D., et al., 2024. A study of hydraulic fracture propagation in

laminated shale using extended finite element method. Comput. Geotech. 166, 105961. https://doi.org/10.1016/j.compgeo.2023.105961.

- De Pater, C.J., Cleary, M.P., Quinn, T.S., et al., 1994. Experimental verification of dimensional analysis for hydraulic fracturing. SPE Prod. Facil. 9 (4), 230–238. https://doi.org/10.2118/24994-PA.
- Dong, X., Zhu, H., Wang, X., et al., 2025. Research and application of hydraulic fracturing fluid entry depth detection method based on water-hammer signal. Geoene. Sci. Eng. 246, 213556. https://doi.org/10.1016/j.geoen.2024.213556.
- Dong, Y., Tian, W., Li, P., et al., 2021. Numerical investigation of complex hydraulic fracture network in naturally fractured reservoirs based on the XFEM. J. Nat. Gas Sci. Eng. 96, 104272. https://doi.org/10.1016/j.jngse.2021.104272.
 Fu, H., Cai, B., Geng, M., et al., 2022. Three dimensional simulation of hydraulic
- Fu, H., Cai, B., Geng, M., et al., 2022. Three dimensional simulation of hydraulic fracture propagation based on vertical reservoir heterogeneity. Nat. Gas. Ind. 42 (5), 56–68 (in Chinese).
- Gao, Q., Cheng, Y., Yan, C., 2020. Numerical study of horizontal hydraulic fracture propagation in multi-thin layered reservoirs stimulated by separate layer fracturing. Geosys. Eng. 23, 13–25. https://doi.org/10.1080/12269328.2018.1515669.
- Guo, P., Li, X., Li, S., et al., 2023. Experimental investigation of simultaneous and asynchronous hydraulic fracture growth from multiple perforations in shale considering stress anisotropy. Rock Mech. Rock Eng. 56, 8209–8220. https://doi.org/10.1007/s00603-023-03499-6.
- Guo, X., Zhu, H., Zhao, P., et al., 2025. Numerical simulation on cross-layer propagation of hydraulic fracture in sand—mud interbedded layers: taking the Shahejie Formation in BZ 25-1 Offshore Oilfield as an example. Rock Mech. Rock Eng. 58, 123—143. https://doi.org/10.1007/s00603-024-03972-w.
- Huang, C., Zhu, H., Wang, J., et al., 2022. A FEM-DFN model for the interaction and propagation of multi-cluster fractures during variable fluid-viscosity injection in layered shale oil reservoir. Pet. Sci. 19 (6), 2796–2809. https://doi.org/ 10.1016/j.petsci.2022.06.007.
- Hou, B., Chen, M., Li, Z., et al., 2014. Propagation area evaluation of hydraulic fracture networks in shale gas reservoirs. Petrol. Explor. Dev. 41, 833–838. https://doi.org/10.1016/S1876-3804(14)60101-4.
- doi.org/10.1016/S1876-3804(14)60101-4.

 Hou, B., Chang, Z., Fu, W., et al., 2019. Fracture initiation and propagation in a deep shale gas reservoir subject to an alternating-fluid-injection hydraulic-fracturing treatment. SPE J. 24, 1839–1855. https://doi.org/10.2118/195571-PA.
- Jiang, T., Zhang, J., Wu, H., 2016. Experimental and numerical study on hydraulic fracture propagation in coalbed methane reservoir. J. Nat. Gas Sci. Eng. 35, 455–467. https://doi.org/10.1016/j.jngse.2016.08.077.
- Li, Q., Xing, H., Liu, J., et al., 2015. A review on hydraulic fracturing of unconventional reservoir. Petroleum 1, 8–15. https://doi.org/10.1016/j.petlm.2015.03.008.
- Liao, S., Hu, J., Zhang, Y., 2024. Mechanism of hydraulic fracture vertical propagation in deep shale formation based on elastic-plastic model. Eng. Fract. Mech. 295, 109806. https://doi.org/10.1016/j.engfracmech.2023.109806.
- Lu, G., Momeni, S., Lecampion, B., 2022. Experimental investigation of hydraulic fracture growth in an anisotropic rock with pre-existing discontinuities under different propagation regimes. In: 56th U.S. Rock Mechanics/Geomechanics Symposium. https://doi.org/10.56952/ARMA-2022-0239.
- Luo, S., Tang, H., Zhang, L., et al., 2024. Efficient optimization of fracturing parameters with consideration of fracture propagation and heterogeneity in tight gas reservoirs. Comput. Geosci. 186, 105563. https://doi.org/10.1016/j.cageo.2024.105563.
- Ma, X., Zou, Y., Li, N., et al., 2017. Experimental study on the mechanism of hydraulic fracture growth in a glutenite reservoir. J. Struct. Geol. 97, 37–47. https:// doi.org/10.1016/j.jsg.2017.02.012.
- Madyarov, A., Prioul, R., Zutshi, A., et al., 2021. Understanding the impact of completion designs on multi-stage fracturing via block test experiments. In: The 55th U.S. Rock Mechanics/Geomechanics Symposium.
- Muther, T., Qureshi, H.A., Syed, F.I., et al., 2022. Unconventional hydrocarbon resources: geological statistics, petrophysical characterization, and field development strategies. J. Pet. Explor. Prod. Technol. 12, 1463—1488. https://doi.org/10.1007/s13202-021-01404-x.
- Ohno, K., Ohtsu, M., 2010. Crack classification in concrete based on acoustic emission. Constr. Build. Mater. 24, 2339–2346. https://doi.org/10.1016/j.conbuildmat.2010.05.004.
- Ou, Y., Liang, H., 2023. Study on the law of hydraulic fracture propagation in low permeability thin interbed reservoir. Engineering 15, 207—219. https://doi.org/10.4236/eng.2023.154016.
- Ouchi, H., Foster, J.T., Sharma, M.M., 2017. Effect of reservoir heterogeneity on the vertical migration of hydraulic fractures. J. Petrol. Sci. Eng. 151, 384–408.

- https://doi.org/10.1016/j.petrol.2016.12.034.
- Qian, Y., Guo, P., Wang, Y., et al., 2020. Advances in laboratory-scale hydraulic fracturing experiments. Adv. Civ. Eng. 2020, 1–18. https://doi.org/10.1155/2020/1386581.
- Ren, Q., Zhang, C., Wu, G., et al., 2024. Hydraulic fracture initiation and propagation in deep coalbed methane reservoirs considering weak plane: CT scan testing. Gas Sci. Eng. 125, 205286. https://doi.org/10.1016/j.jgsce.2024.205286.
- Sun, K., Zhang, S., Xin, L., 2016. Impacts of bedding directions of shale gas reservoirs on hydraulically induced crack propagation. Nat. Gas. Ind. 36 (2), 45–51 (in Chinese).
- Sun, K., Ji, H., Zhang, S., 2020. Influence of bedding azimuth and strength on hydraulic fracturing in shale. J. Exp. Mech. 35 (2), 343–348 (in Chinese).
- Tan, P., Jin, Y., Han, K., et al., 2017. Analysis of hydraulic fracture initiation and vertical propagation behavior in laminated shale formation. Fuel 206, 482–493. https://doi.org/10.1016/j.fuel.2017.05.033.
- Tang, X., Zhu, H., Zhao, P., et al., 2024. A numerical study of complex fractures propagation path in naturally fractured gas shale: Reorientation, deflection and convergence. Gas Sci. Eng. 121, 205186. https://doi.org/10.1016/i.jessce.2023.205186.
- Wang, E., Zhu, H., Yi, X., et al., 2025. Numerical simulation of fracture propagation in high-energy gas fracturing of shale reservoir. Geoenergy Sci. Eng. 252, 213915. https://doi.org/10.1016/j.geoen.2025.213915.
- Wang, F., Liu, W., Deng, J., et al., 2024. Hydraulic fracture propagation research in layered rocks based on 3D FEM modeling and laboratory experiments. Geoene. Sci. Eng. 234, 212670. https://doi.org/10.1016/j.geoen.2024.212670.
- Warpinski, N.R., Teufel, L.W., 1987. Influence of geologic discontinuities on hydraulic fracture propagation. J. Petrol. Technol. 39 (8). https://doi.org/10.2118/13224-PA
- Wu, S., Ge, H., Li, T., et al., 2022. Characteristics of fractures stimulated by supercritical carbon dioxide fracturing in shale based on acoustic emission monitoring. Int. J. Rock Mech. Min. Sci. 152, 105065. https://doi.org/10.1016/ i.ijrmms.2022.105065.
- Yang, L., Sheng, X., Zhang, B., et al., 2023. Propagation behavior of hydraulic fractures in shale under triaxial compression considering the influence of sandstone layers. Gas Sci. Eng. 110, 204895. https://doi.org/10.1016/i.igsce.2023.204895.
- Yu, B., Liu, C., Chen, W., et al., 2022. Experimental study on deformation and fracture characteristics of coal under different true triaxial hydraulic fracture schemes. J. Petrol. Sci. Eng. 216, 110839. https://doi.org/10.1016/j.petrol.2022.110839.
- Yu, J., Li, N., Hui, B., et al., 2024. Experimental simulation of fracture propagation and extension in hydraulic fracturing: a state-of-the-art review. Fuel 363, 131021. https://doi.org/10.1016/j.fuel.2024.131021.
- Zeng, Q., Bo, L., Li, Q., et al., 2023. Numerical investigation of hydraulic fracture propagation interacting with bedding planes. Eng. Fract. Mech. 291, 109575. https://doi.org/10.1016/j.engfracmech.2023.109575.
- Zhai, L., Xun, Y., Liu, H., et al., 2023. Experimental study of hydraulic fracturing initiation and propagation from perforated wellbore in oil shale formation. Fuel 352, 129155. https://doi.org/10.1016/j.fuel.2023.129155.
- Zhang, F., Wu, J., Huang, H., et al., 2021. Technological parameter optimization for improving the complexity of hydraulic fractures in deep shale reservoirs. Nat. Gas. Ind. 41 (1), 125–135 (in Chinese).
- Zhang, Y., Long, A., Zhao, Y., et al., 2023. Mutual impact of true triaxial stress, borehole orientation and bedding inclination on laboratory hydraulic fracturing of Lushan shale. J. Rock Mech. Geotech. Eng. 15, 3131–3147. https://doi.org/10.1016/j.jrmge.2023.02.015.
- Zhao, P., Zhu, H., Li, G., et al., 2024. Large-scale physical simulation of injection and production of hot dry rock in Gonghe Basin, Qinghai Province, China. Petrol. Explor. Dev. 51, 741–752. https://doi.org/10.1016/S1876-3804(24)60502-1.
- Zhao, Y., Zhang, Y., He, P., 2023. Hydraulic Fracturing and Rock Mechanics. Springer Nature Singapore, Singapore. https://doi.org/10.1007/978-981-99-2540-7.
- Zhao, Z., Li, X., Wang, Y., et al., 2016. A laboratory study of the effects of interbeds on hydraulic fracture propagation in shale formation. Energies 9, 556. https://doi.org/10.3390/en9070556.
- Zhou, Z., Hou, Z., Guo, Y., et al., 2024. Experimental study of hydraulic fracturing for deep shale reservoir. Eng. Fract. Mech. 307, 110259. https://doi.org/10.1016/ j.engfracmech.2024.110259.
- Zhu, H., Gong, D., Zhang, B., 2023. A multi-scale geology-engineering sweet spot evaluation method for tight sandstone gas reservoirs. Nat. Gas. Ind. 43 (6), 76–86. https://doi.org/10.1016/j.ngib.2023.09.007.